RESEARCH PAPER

PCCP
www.rsc.org/pccp

Electro-oxidation of carbon monoxide and methanol on bare and Pt-modified Ru(10$\bar{1}$0) electrodes

A. L. N. Pinheiro,*[a] M. S Zei[b] and G Ertl[a]

[a] *Fritz Haber Institut der Max Planck Gesellshaft, Faradayweg 4-6, D-14195 Berlin, Germany. E-mail: pinheiro@fhi-berlin.mpg.de; Fax: +49 30 8413 5106; Tel: +49 30 8413 5141*
[b] *Department of Physics, National Central University, 32054 Jungli, Taiwan*

Received 26th July 2004, Accepted 20th January 2005
First published as an Advance Article on the web 7th February 2005

The activity towards CO and methanol electrooxidation of bare and platinum-modified Ru(10$\bar{1}$0) surfaces has been investigated. The structure/morphology and composition of the modified surfaces were characterized using electron diffraction techniques (LEED, RHEED) and Auger spectroscopy. The bare Ru(10$\bar{1}$0) surface exhibits a higher catalytic activity towards CO electrooxidation than the Ru(0001) surface due to the lower oxidation potential of the former surface. The early stages of surface oxidation lead to disordering of the surface and further enhancing of the electrocatalytic activity. Electrodeposition of Pt on Ru(10$\bar{1}$0) leads to epitaxial growth *via* a Volmer–Weber growth mode. The Pt clusters grow preferentially with the (311) plane parallel to the substrate surface with (0$\bar{1}$1) rows in the layers in contact with the substrate compressed by about 3% with respect to bulk Pt, in order to match with the (12$\bar{1}$0) rows of the Ru(10$\bar{1}$0) surface. This compression leads to enhanced catalytic activity towards CO oxidation for thin Pt deposits whereas for large deposited Pt particles the dominating factor for the catalytic enhancement is the higher concentration of surface defects. On the other hand, in the case of methanol oxidation, the dominant factor in determining the catalytic activity is the concentration of adjacent Pt–Ru sites, although surface defects play an important role in the methanol dehydrogenation steps.

Introduction

The most widespread and promising anodes for fuel cell (FC) applications employ dispersed metal nanoparticles as the electrocatalyst, usually a platinum based alloy, and reformed hydrogen or methanol as fuels.[1] CO can be formed at the anode as a poisoning intermediate in the case of DMFC (direct methanol fuel cell) or is introduced into the system as a contaminant present in the reformed hydrogen. Pure platinum catalysts are not efficient anodes in this context because of the high potential required to effectively oxidize CO. This has been attributed to the fact that adsorbed oxygen-containing species can only be formed at high potentials on platinum. Bi-metallic Pt catalysts, mainly Pt–Ru,[2–15] but also Pt–Sn,[16] Pt–Mo[17] and Pt–Os[18] have been intensively studied in order to overcome this problem. The underlying idea is the so-called bi-functional mechanism with the less noble foreign metal providing sites for the formation of oxygen-containing species at lower potentials.[19,20] The determination of the optimum ratio in bi-metallic catalysts has so far been achieved by trial and error. This is mainly because the real-world catalyst is a complex system which hinders a reliable theoretical approach. The main problems arise from the lack of control of the morphological characteristics, particle size distribution and chemical composition of the prepared catalyst. In this context, well defined surfaces used as model systems have been employed to overcome this problem, which can be tailored to mimic the real-world catalysts while keeping controlled characteristics. In the case of Pt/Ru alloys, where the two elements are distributed on the surface, the optimum Pt/Ru ratio for CO electrooxidation of 50%[21–23] differs from that for the methanol oxidation which lies in the range of 10–40%.[24–26] This has been attributed to the fact that the first steps of methanol electrooxidation involve the adsorption/dehydrogenation of methanol on platinum sites. Apparently, this process requires tri-coordinated Pt sites[22,23] and the probability of the occurrence of these sites increases with the Pt content. These interpretations are in accordance with the bi-functional mechanism. However, a further complication to this scenario comes from the observation of changes in the CO binding energy for the bi-metal system with respect to the individual metals.[27] The importance of this effect, so-called electronic effects, has been recognized in the theoretical work by Nørskov[28] correlating the d-band center with the adsorption energy and its implication in the catalytic activity of metal surfaces. These theoretical predictions matched well when applied to binding energy of CO adsorbed on transition metal surfaces.[29] This same phenomenon seems to underlie the effect of surface defects on the catalytic activity: The defects provide highly active surface atoms of lower coordination number, which contribute to a shift in the d-band center.[30]

In the distributed Pt–Ru alloy systems it is difficult to experimentally determine the relative contributions of the electronic effects and the bi-functional pathway to the promotion of electrocatalytic activity. Shubina and Koper[31] have used DFT calculations to determine the extent of electronic effects on the binding energy of CO and OH on Pt and Ru sites for Pt–Ru alloy and overlayer systems. Experimentally, this effect can be better investigated in overlayer systems. However, purely electronic effects can be discussed only in the case of complete overlayers, otherwise oxidation *via* the bi-functional route can occur at the substrate–overlayer perimeter. In this sense, characterization of the epitaxial growth of metal overlayers is required in order to understand the electrocatalytic activity of the bi-metallic system.[32] The epitaxial growth of metal adlayers can lead to admetal–admetal distances different from the bulk metal value to match the structure of the ordered single crystal substrates, at least in the first few layers. This lattice compression/expansion causes strain in these adlayers which also leads to electronic effects.[33,34] Experimental and theoretical studies on Pt pseudomorphic overlayers on

DOI: 10.1039/b411467a

Ru(0001) by Schlapka *et al.*[35] have shown that the electronic effects on the Pt–CO binding energy arise both from the substrate interactions and lattice compression. These authors concluded that the electronic effects due to substrate interactions are of short range, vanishing for thicknesses greater than three monolayers (ML). On the other hand, the effects due to the lattice compression was found to extent to considerably thicker films as the relaxation of Pt–Pt lattice constant towards the bulk value started to become noticeable only around 8 ML film thickness. The same effect was used to explain the lower binding energy of Pt–H in pseudomorphic Pt overlayers on Ru(0001).[36]

In the following, results of the electrocatalytic activity towards CO and methanol oxidation of platinum adlayers electrochemically grown on the $(10\bar{1}0)$ face of a ruthenium single crystal are presented. An attempt is made to correlate these results with the surface structure/morphology determined by employing electron diffraction techniques, namely, low energy electron diffraction (LEED) and reflection high energy electron diffraction (RHEED) and surface composition, determined by Auger electron spectroscopy (AES). Studies on the bare Ru$(10\bar{1}0)$ surface towards CO electrooxidation were also carried out as this plane has so far been only rarely investigated in electrocatalysis.[15,37–39] It has, however, been studied in UHV in the field of heterogeneous catalysis,[40–45] concerning the CO oxidation reaction. In this case, bare Ru is found to be quite inactive for the CO oxidation when compared to other late transition metals, whereas an increase in the catalytic activity is observed at high pressure associated with the formation of ruthenium dioxide.[45–47] A higher catalytic activity of Ru$(10\bar{1}0)$ compared with the Ru(0001) surface can be inferred from the fact that the formation of RuO_2 is more facile in the more open structure of the $(10\bar{1}0)$ surface.[45] The same trend was observed by Brankovic *et al.* in the electrochemical environment,[15] but still few results are available in the electrochemistry literature for the Ru$(10\bar{1}0)$ compared with the (0001) surface.[11,36,37,48–59]

Experimental

The experiments were performed with a system consisting of an UHV chamber with base pressure $< 1.5 \times 10^{-10}$ mbar equipped with LEED, RHEED and a spherical sector (150°) Auger detector. The UHV chamber was also equipped with the facilities for sample cleaning by Ar^+ sputtering, and a closed sample transfer to an electrochemical cell. The cell was assembled at the top of a capillary which was introduced into the electrochemical chamber after prior ventilation with high purity argon gas. A platinum coil was used as counter-electrode and the $Ag/AgCl/KCl_{sat}$ as reference electrode, with respect to which all the potential values are referred throughout this paper.

RHEED experiments were performed with an incident electron beam of 38 keV energy at grazing angles (1–2°) to the surface. The same beam was used as a primary excitation source for the Auger experiments.

The working electrode, a Ru$(10\bar{1}0)$ single crystal disk of 8 mm in diameter (0.5 cm^2), cut and polished in-house, was mounted between tungsten wires through side slits on the sample. The tungsten wires also served for the resistive heating of the sample. The sample treatment in the UHV chamber consisted of several cycles of Ar^+ (5×10^{-5} mbar) sputtering at 1.0 keV with the sample heated at 1100 K for 20 min and subsequent annealing at 1300 K.

The $HClO_4$ 0.1 M and CH_3OH 0.1 M/$HClO_4$ 0.1 M working solutions were prepared using reagent grade water from a Milli-Q system and high quality chemicals $HClO_4$ (Suprapure, Merck) and Methanol (PA, Merck). Prior to the electrochemical experiments, the solutions were previously purged with 99.999% N_2 for at least 1 h. The $HClO_4$ 0.1 M solution was saturated with high purity CO (99.999%), when required, by bubbling for no less than 20 min, after the N_2 purging.

The electrochemical equipment used was an in-house built potentiostat (ELAB, Fritz-Haber Institut) and the signal was recorded using a multi-channel AD converter board by Meilhaus and in-house written software.

Results and discussion

Bare Ru$(10\bar{1}0)$

LEED from the freshly prepared Ru$(10\bar{1}0)$ shows a sharp (1 × 1) phase as presented in Fig. 1(a); however, this can only be observed in a small part of the Ru electrode surface, while most of the Ru surface (90%) shows a streaked LEED pattern with spot intensity elongation along the $[\bar{1}2\bar{1}0]$ direction as in Fig. 1(b). UHV studies revealed that the presence of adsorbed oxygen leads to a missing row (1 × 2) pattern streaked along the [0001] direction[45] but this can be ruled out in the present case as no oxygen signal could be identified in the Auger spectrum for this sample. This streaking is indicative of the absence of long range order along the $[\bar{1}2\bar{1}0]$ direction on the Ru$(10\bar{1}0)$ surface. The streaking of the LEED pattern is attributed to the presence of domain walls (antiphase domain boundaries) along the [0001] direction perpendicular to the $[\bar{1}2\bar{1}0]$ direction. The domain walls may arise from discontinuities in the Ru crystal.[60]

The spacing between the (00) and (10) beams in RHEED (Fig. 1(c)) at the [0001] azimuth is the reciprocal unit vector b_{10} (0.396 $Å^{-1}$) of a two-dimensional (2D) reciprocal unit mesh of Ru$(10\bar{1}0)$ as denoted by the 10 spot in LEED, corresponding to the reciprocal value of the [0001] atomic row spacing (2.706 Å) of the Ru$(10\bar{1}0)$ surface. The reflection streak spacing at the $[\bar{1}2\bar{1}0]$ azimuth is b_{01} (0.233 $Å^{-1}$) corresponding to the 01-LEED spot (Fig. 1(d)). The partial disorder on the Ru$(10\bar{1}0)$ surface is also evidenced by the broad reflection streak in RHEED at the [0001] azimuth (Fig. 1(c)), while at the $[\bar{1}2\bar{1}0]$

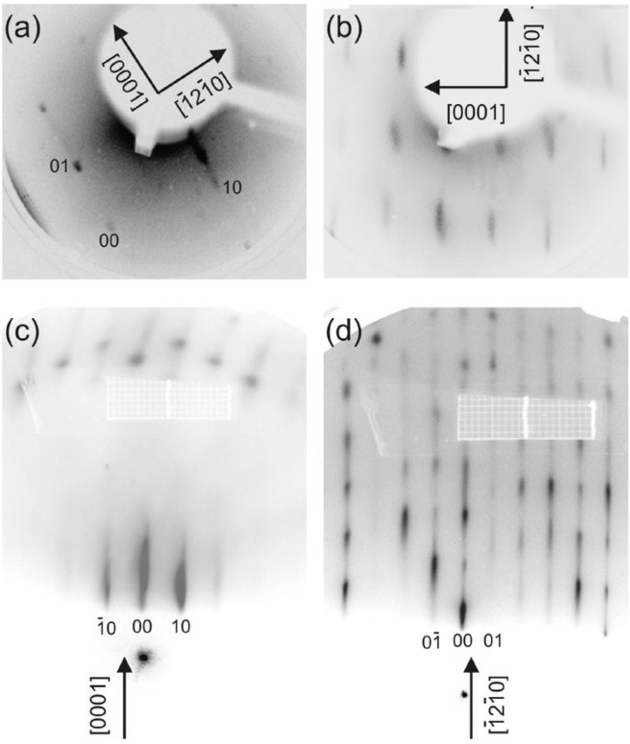

Fig. 1 LEED patterns for the clean Ru$(10\bar{1}0)$ prepared in UHV at two different regions of the sample: well ordered region, −55 eV (a), and predominant region showing streaky spots due to domain walls perpendicular to the [0001] direction, −120 eV (b). RHEED pattern in the same region as in (b) with the incident beam in the [0001] (c) and $[\bar{1}2\bar{1}0]$ (d) azimuths, respectively.

azimuth (Fig. 1(d)) the streaks are sharper, indicating better order between the $[\bar{1}2\bar{1}0]$ atomic rows. However, a lack of long range order along these rows is reflected in the fact that the streaks are spanned all over between the 0th and 1st Laue zones and exhibit intensity modulation.[54,61] The imperfection of the Ru crystal can be partially removed by cycles of argon ion sputtering and annealing as demonstrated by the reduced spot-streaking in the LEED pattern; however, they cannot be completely eliminated. The reason for the misfit formation during the crystal growth leading to the domain walls in the Ru crystal is so far not clear.

The cyclic voltammograms (CVs) of the Ru(10$\bar{1}$0) surface in 0.1 M perchloric acid are shown in Fig. 2(a) for several upper/lower potential limits. In the positive going scan, the voltammograms feature a peak at about −100 mV and a shoulder in the vicinity of 300 mV. If the lower limit is extended too far into the hydrogen discharge region, the former peak seems to be slightly shifted towards more positive values and is superimposed on a large background current due to the hydrogen reduction. This shift is probably due to a local pH change next to the surface region as a result of the hydrogen discharge processes. In the negative going scan the CVs show features which strongly depend on the upper limit potential. A peak is always observed at −190 mV superposed on a background cathodic current which increases as the upper potential limit is made more positive. This peak is the cathodic counterpart of the anodic peak at −100 mV, as the latter disappears if the lower limit is made more positive than *ca.* −150 mV whilst the remaining features are kept. Next, a rather small spike at −50 mV, which has no anodic counterpart, can be observed if the upper limit exceeds 300 mV. Also, around 200 mV, a broad shallow peak becomes apparent whose center shifts towards more negative potentials upon increasing the upper potential limit. For upper potential limits above 600 mV the current density increases rapidly, probably due to early stages of bulk oxide formation, and the oxide reduction peak is shifted towards even more negative potentials, masking the spike at −50 mV. In fact, after a few incursions into the region above 600 mV the general profile of the CVs changes irreversibly, and it cannot be recovered by further decreasing the upper and lower potential limits. As a result (Fig. 2(b)), the otherwise sharper features of the CVs are no longer identifiable and the small spike at −50 mV cannot be recovered. However, the current density does not change appreciably, suggesting that these irreversible changes in the CV profile are related to disordering of the surface instead of an increase in the surface area by roughening. The spike at −50 mV can be assigned then to the presence of surface ordering.

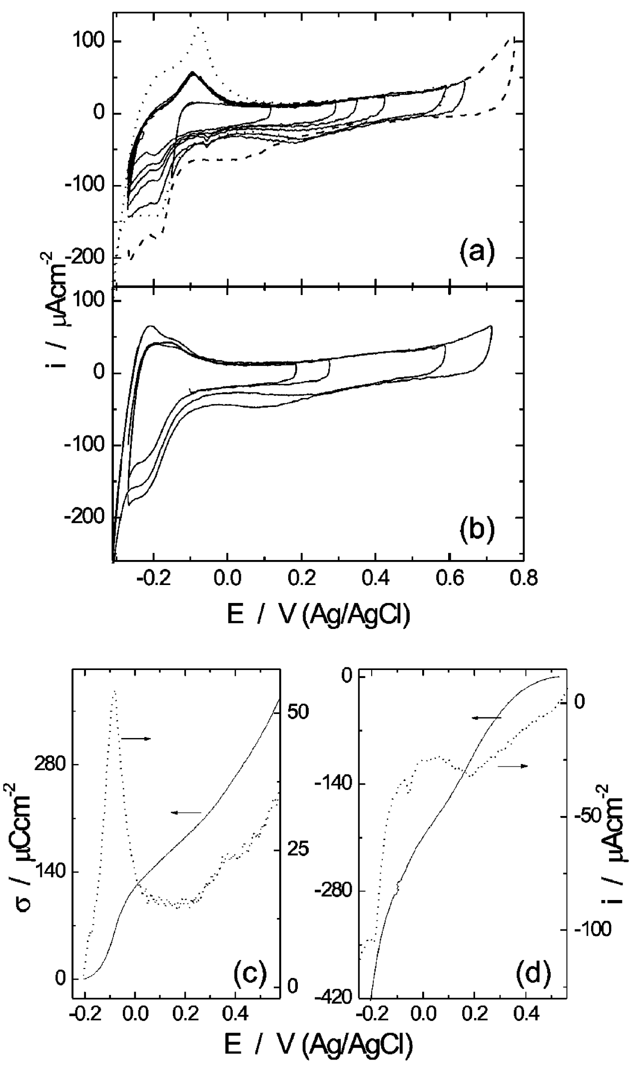

Fig. 2 Cyclic voltammograms of the clean Ru(10$\bar{1}$0) in 0.1 M $HClO_4$ for different upper/lower potential limits for the freshly prepared sample (a) and after extending the upper potential limit into the oxide region (b). Charge obtained by integration of the cyclic voltammogram for the freshly prepared sample in the positive (c) and negative (d) going scan. Scan rate 50 mV s^{-1}.

In order to better ascribe the possible surface processes taking place to the features observed in the CVs, the charge density obtained by integration of the CV in the potential region between −270 and 600 mV are shown in Fig. 2(c) and (d) for the positive and negative going scan, respectively. The respective current density curves are also shown in these figures on a magnified scale. The total charge in the positive going scan amounts to ~380 μC cm^{-2}, which corresponds to 2.6 electrons per surface atom (1 electron per atom corresponds ideally to ~140 μC cm^{-2} for a perfectly smooth surface) after correction for the charging of the double layer, assumed to be about 20 μC cm^{-2} in this potential interval (assuming a capacity of about 20 μF cm^{-2} for a purely capacitive process). Approximately 0.9 electrons per atom are transferred by the end of the peak at −100 mV, a further 0.8 in the intermediate region up to 300 mV and another 0.9 up to 600 mV. In the negative going scan, as much as 1.6 electrons per atom are transferred in the region of the broad reduction peak to −50 mV where the spike appears. Beyond this potential it is not possible to determine the amount of adsorbed charge (corresponding to the peak at −190 mV) as it seems to be superposed on the current due to hydrogen discharge. The charge associated with the latter faradaic process might also be masking some possible anodic process in the potential region below the first anodic peak as it is impossible to determine a proper baseline for integration in this region.

Characterization of the individual processes contributing to the CV features is still under dispute. In the case of Ru(0001), several reports[48,49,51,53] have assigned the first peak to hydrogen desorption, while CO charge displacement experiments by El Aziz and Kibler[56] lead these author to ascribe this peak to OH^- adsorption whilst a peak due to hydrogen-upd can only be observed at lower potentials, in the hydrogen discharge region. The existence of H-upd on Ru(0001) at lower potential has been confirmed also by Hoster *et al.*[36] In the case of Ru(10$\bar{1}$0) in sulfuric acid solution, Brankovic *et al.*,[15] using the same technique, determined a cathodic charge displaced by CO and associated it with OH^-. By associating the first peak with OH^- adsorption up to nearly a monolayer, further surface oxidation must account for 1.6 electrons per surface atom, amounting to 2.6 electrons per surface atom for the overall oxidation process. It is possible that, due to the open structure of the Ru(10$\bar{1}$0) surface, the Ru atoms on the second layer are also taking part in the oxidation process. It would then take about 0.3 monolayers of the second Ru layer to account for the excess charge density. From UHV studies it is known that oxygen adsorption on Ru(10$\bar{1}$0) below 1 ML occurs at the hcp three-fold sites,[42–44] forming zigzag chains, with c(2 × 4)-2O structures at low coverages and (2 × 1)-p2mg-2O at high coverages. Therefore, oxygen is attached to 2 Ru atoms in the first layer and one Ru in the second layer. For oxygen coverages above 1 ML,[45] a streaky (1 × 2) structure was observed in LEED, associated with the initial stages of the RuO_2 formation. This is concomitant with the appearance of an extra peak in the oxygen thermal desorption spectrum at slightly higher temperature with respect to that of the 1 ML (2 × 1)-p2mg-2O structure. It is possible that a similar process is occurring in the electrochemical environment. This similarity in the oxygen adsorption in the electrochemical and gas phase environments has been observed for the case of Ru(0001).[37] Here, we adopt this latter view and associate the peak at −100 mV in the positive going scan with OH^- adsorption. Further evidence will be presented in the following discussion of the CO stripping curves. Above 300 mV, after close to one monolayer of adsorbed oxygen is formed, further oxidation of the surface takes place leading to the formation of a second oxygen phase. If this second oxygen phase causes disorder of the surface to some extent, the spike at −50 mV can be assigned to an order/disorder transition induced by the oxide reduction.

CO oxidation on bare Ru(10$\bar{1}$0)

CO stripping curves are shown in Fig. 3(a) for different experimental conditions. In all cases, the CO electrosorption on Ru(10$\bar{1}$0) was conducted in CO-saturated 0.1 M $HClO_4$ at −200 mV for 3 min. The CO-free solution was then fluxed through the capillary cell, delivered from a secondary cell compartment. During this procedure, the potential was kept at −200 mV. The solution exchange was performed for no less then 2 min before starting the CO oxidative stripping, to ensure a CO-free electrolyte. The efficiency of this procedure can be verified by recovery of the bare Ru CV profile in the potential region between −0.2 and 0.2 V and the absence of CO oxidation current in the subsequent potential cycle. The solid curve was obtained with a sample freshly prepared in UHV while the dotted curve was obtained after potential cycling in the base solution in the same potential range. The dashed curve was obtained with the freshly prepared sample also, but after only one cycle of ion sputtering/annealing as a repetition of the first experiment. In the first case, two partially overlapping peaks can be seen during the CO stripping at 380 and 520 mV, respectively. In the second case only a broad peak with a maximum at around 395 mV can be observed similar to that observed for the CO oxidative stripping on the polycrystalline Ru.[21–23] For the dashed line, the first peak is observed at 395 mV also, but the second peak is still clearly discernible. The change in the peak potential seems to be only an artifact of the coupling of the two peaks. In all cases the CO layer seems to be completely oxidized during the first scan. Also, in the case of the freshly prepared sample, the spike at −50 mV is pronounced and sharp (inset of Fig. 3(a)) and the CV profile in the more negative region changes. Not only is the cathodic peak at −190 mV less pronounced for the case of the previously cycled sample but also a second cathodic peak around −250 mV appears.

Despite the differences in the profile of the CO stripping curves, the overall charge involved in this process amounts to nearly the same value, *ca.* 630 (freshly prepared sample) to 640 (previously cycled sample) $\mu C\ cm^{-2}$ which would yield a four electrons per surface atom process. Again, the main difference seems to be more related to differences in ordering then roughening. This can be seen in Fig 3(b), where the CO stripping curves are shown for two samples deliberately roughened by ion sputtering. The CO oxidation peak is negatively shifted by about 40 mV for the case of the rough samples. This enhancement of CO oxidation due to roughening of the surface has been observed in the case of Pt(111) and Ru(0001)[54] and this enhancement is due to the earlier formation of oxygenated species on the rough surface. Under UHV conditions, CO adsorbs on Ru(10$\bar{1}$0) in an on-top configuration up to 1 ML,[40] reaching a saturation coverage of 1.25 ML, with the excess CO adsorbed in a bridge-bonded configuration. Assuming the same behavior in the electrochemical environment, the hcp three-fold sites are left free for the adsorption of oxygen-containing species (either O or OH). This being the case, the onset of formation of oxygenated species in the rough surfaces is shifted towards more negative potentials as the O/OH are more easily adsorbed at the defects and steps/kinks of the rough surfaces.

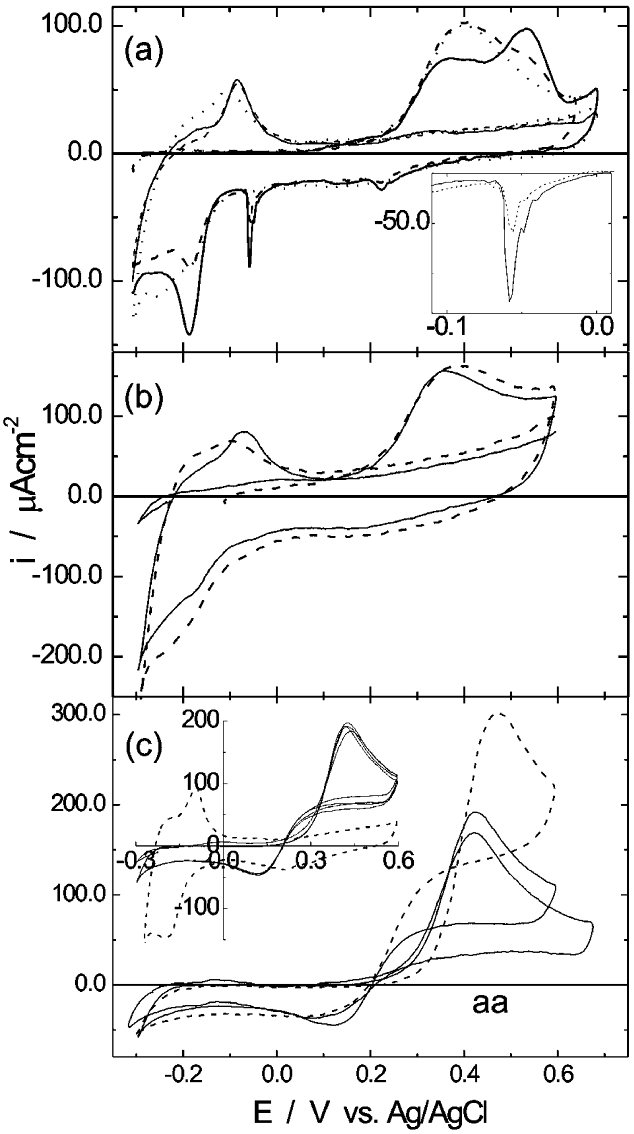

Fig. 3 CO Oxidative stripping curve on Ru(10$\bar{1}$0) after CO electrosorption at −0.2 V for the smooth surface freshly prepared sample in UHV (—) and (--); and previously cycled in the base solution (···) (a). The same experiment using two roughened Ru(10$\bar{1}$0) samples (b). Cyclic voltammograms (third cycle) of the Ru(10$\bar{1}$0) in CO_{sat} 0.1 M $HClO_4$ for the quiescent solution (—) and with assisted mass transport (--) (c); inset: cycles 1–4 of the cyclic voltammogram for the quiescent solution (dashed line: CO-free solution). Scan rate 50 mV s^{-1}.

The charge involved in the CO stripping process, a two electrons per molecule process, would correspond to half of the overall charge evaluated from the curves in Fig. 3(a) for the stripping of 1 ML. The other half is obviously related to the further ruthenium oxidation process.[21] The CO stripping takes place at potential above 300 mV, where the CO-free surface would be completely oxidized as discussed before. The presence of CO on the surface inhibits the (hydr)oxide formation at lower potentials. After the CO molecules leave the surface, it is made available for further oxidation:

$$\text{Ru–CO} + \text{Ru(Ox)} \rightarrow \text{CO}_2 + 2\text{Ru} \overset{\text{H}_2\text{O}}{\rightarrow} 2\text{Ru(Ox)} + ne^- + n\text{H}^+ \qquad (1)$$

This is evident from the fact that the cathodic charge in the negative going scan is almost the same for both the first and second cycles. This indicates that, to a good approximation, at the end of the positive going scan, the surface oxidation state is the same, irrespective of the previous presence of CO. In the second cycle, the overall charge in the positive going scan, including the peak at −100 mV, would sum up to approximately 330–400 μC cm^{-2} for the three CVs of Fig. 3(a), which leaves about 240–300 μC cm^{-2}, or ~2 electrons per surface atom, for the oxidation of 1 ML of CO.

If the first anodic peak in the second cycle were associated with hydrogen desorption only, an extra 150 μC cm^{-2} would have to be assigned to the process of CO oxidation. This would exceed the amount of CO by approximately half a monolayer, unless a roughness factor of 1.5 is assumed. It thus reinforces the conclusion that the first anodic peak at −100 mV is partially due to the surface oxidation. The appearance of a second peak during the CO stripping experiment is assigned to the coupling of the CO oxidation and a further Ru oxidation at the CO-free part of the surface. These two processes can be better resolved as the surface is better ordered, which implies that the surface oxide formation involves a slower step compared with the CO oxidation on a more ordered surface. In the case of the less ordered surface, these two processes overlap resulting in a broad peak. As discussed earlier, a second oxygen phase starts to form only above 300 mV in the CO-free solution. This suggests that the CO is only oxidized after some oxygenated species is adsorbed with characteristics similar to that of the second oxygen phase. This process takes place at significantly lower potential on the more open structure of the Ru(10$\bar{1}$0) than on Ru(0001), leading to the improved catalytic activity of the former surface towards CO electrooxidation. The nature of this second oxygen phase is still unclear. Brankovic *et al.*[15] used the concept of sub-surface oxygen to account for this catalytic enhancement. In the negative going scan, the order/disorder transition associated with the spike at −50 mV is more pronounced in the case of the more ordered surface (the freshly prepared sample). For the case of the sample previously cycled, the surface is already lacking in long-range order and no transition takes place at all.

The third cycle of the CV of the Ru(10$\bar{1}$0) in contact with CO-saturated 0.1 M $HClO_4$ is presented in Fig. 3(c). The CO oxidation current at the peak is ~200 μA cm^{-2} at 50 mV s^{-1} which agrees with the value reported for polycrystalline Ru in 0.05 M H_2SO_4[50] (~70 μA cm^{-2} at 20 mV s^{-1}) and is considerably smaller than the value reported for Ru(10$\bar{1}$0) 0.1 M H_2SO_4[15] (~250/160 μA cm^{-2} at 20 mV s^{-1}). The CO oxidation peak can be seen at 420 mV, about 30 mV shifted positively with respect to the CO stripping curve. The same shift is also observed for the onset of CO oxidation. This happens due to CO re-adsorption and, possibly also to additional CO adsorption at the threefold hcp sites, which blocks the surface and inhibits the formation of oxygenated species. The aforementioned effect becomes evident by the fact that the potential is further shifted if the mass transport is assisted (by fluxing the electrolyte – dashed line). This has been observed by Gasteiger *et al.*[22] in the case of Pt and Pt–Ru 50:50 alloy electrodes and associated to a weaker bonded OH_{ads} on these surfaces. This makes the process very sensitive to mass transport conditions due to the strong competition for adsorption sites between CO and OH^-. This competition accounts for the hysteresis observed in the CV. However, in the same work, the authors observed no pronounced mass transport sensitivity for the CO electro-oxidation on polycrystalline Ru and attributed this to the strongly bonded OH_{ads} on bare Ru. Fig. 3 shows a different behavior for the Ru(10$\bar{1}$0). The Ru oxidation scheme discussed above involving a second oxygen phase can also explain the behavior of Fig. 3(c), in a way very similar to the mechanism proposed for the gas phase CO oxidation on the RuO_2(100) grown on Ru(10$\bar{1}$0).[45–47] This involves the reaction of CO adsorbed in the on-top position with a first type of adsorbed oxygen. However, a second type of oxygen also plays an important role as soon as the first type of oxygen is consumed by CO oxidation. Accordingly, it is proposed for the present case, that CO can react preferably with the second oxygen phase. CO re-adsorption from the solution inhibits the formation of the first oxygen phase. This way, the same behavior as in the case of platinum can be expected. The ability of the CO to displace the first oxygen phase can be observed in the negative going scan: the carbon monoxide oxidation comes to a halt in the region between 300 mV and 200 mV because no second adsorbed oxygen phase can be formed any longer. At this point, due to the low concentration of CO at the interface, the surface is covered by the first oxygen phase. The CO concentration at the surface then builds up again, and CO re-adsorbs onto the surface displacing the adsorbed oxygen. The displaced adsorbed oxygen takes two electrons per atom to leave the surface. This explains the slightly larger cathodic current density between 160 and 0 mV observed in the negative going scan for the CO-saturated solution than in the CO-free solution. As much as 300 μC cm^{-2} (~2 e$^-$ per atom) are transferred from 200 mV down to the lower potential limit, on average, for each case of Fig. 3(b). Although this is a rough estimation as faradaic processes might be superposed at the considered limits, it allows one to infer that a considerable amount of oxygenated species is displaced below 200 mV due to CO re-adsorption. The presence of OH^- alone cannot account for the amount of charge displaced.

The presence of strongly adsorbed OH on polycrystalline Ru[22] and also on Ru(10$\bar{1}$0)[15] has been postulated to explain the poisoning for the CO oxidation at more positive potentials. The CV in the solid line of Fig. 3(c) suggests the same. However, it is also possible that this behavior is, in part, related to fluctuactions in CO diffusion to the interface, at least in the potential range investigated here. The mass transport conditions are ill defined for the case of the quiescent electrolyte. The inset of Fig. 3(c) shows the four first cycles of the CV for the quiescent CO-saturated solution. Variations in the current density in the plateau can also be observed at each cycle without changing the upper limit potential. These variations are not observed under the more defined mass transport conditions obtained with the flowing electrolyte. Real steady state polarization curves, where no diffusion layer relaxation takes place, would be required to unambiguously evaluate the extent of the poisoning effect of strongly bonded oxygenated species. For the case of the very positive potentials, as discussed in ref. 15, this effect is probably due to the formation of catalytically inactive Ru oxides.[12,14,45–47]

After the electrochemical experiments, the electrode was emersed at −200 mV and ordered LEED or RHEED patterns were no longer discernible, indicating the loss of the long-range order of the surface. The sample was then flashed in UHV at a temperature below 400 °C for 2 min and the LEED pattern obtained at 55 eV is shown in Fig. 4(a). The LEED pattern at the same energy for the clean Ru(10$\bar{1}$0) after ion bombardment and annealing is shown in Fig. 4(b) for comparison. Fig. 4(a) shows streaks along the ($\bar{1}2\bar{1}0$) direction as before and also the appearance of a (1 × 4) structure. This reflects either the presence of some strongly bonded oxygen overlayer not desorbed below 400 °C or the fact that the surface had undergone a reconstruction during the electrochemical experiments or during the flashing. The Auger spectrum after flashing the sample showed no oxygen signal, but it might be present below the detection limit for Auger. It is not possible therefore to

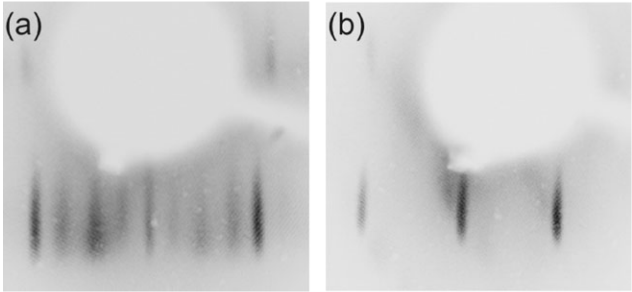

Fig. 4 LEED patterns for sample after electrochemical experiment and subsequent flashing below 400 °C (a) and after cleaning and annealing in UHV (b); 55 eV.

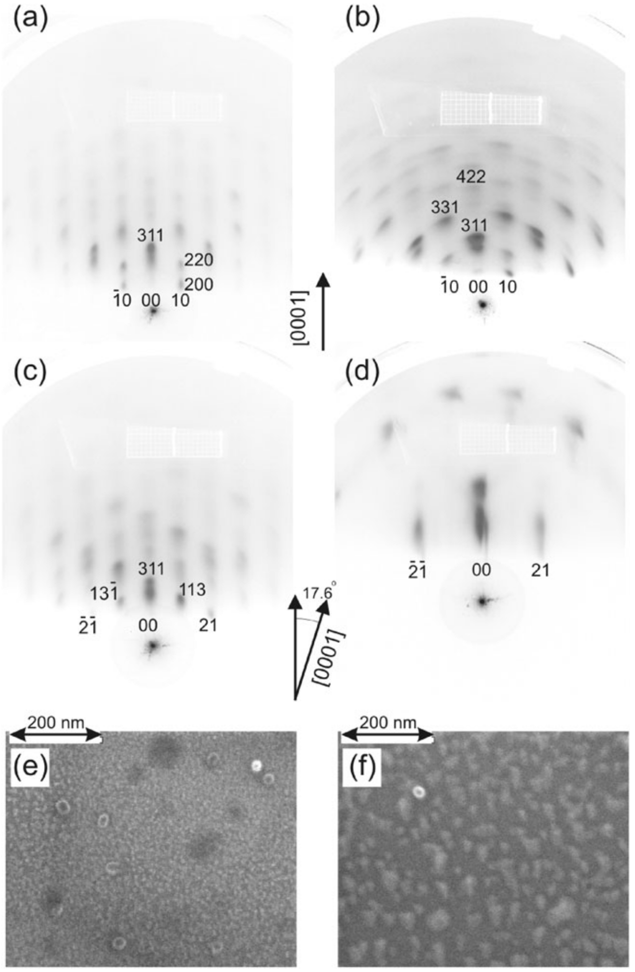

Fig. 5 RHEED patterns with incident beam in the [0001] direction for the potentiostatically (a) and potentiodynamic (b) Pt-modified Ru(10$\bar{1}$0). For the incident beam rotated ~17° w.r.t. the [0001] direction for the potentiostatically modified (c) and bare Ru(10$\bar{1}$0) (d). SEM images for the potentiostatically (e) and potentiodynamic (f) Pt-modified Ru(10$\bar{1}$0).

unambiguously interpret this result, but it is obvious that during the electrochemical experiments the surface undergoes major structural changes. This phenomenon of enhanced surface atoms mobility induced by adsorption – electrochemical annealing – has been reported before[48] for the case of Ru(0001) upon CO adsorption.

Pt deposition on Ru(10$\bar{1}$0)

Platinum was deposited on Ru(10$\bar{1}$0) using two different methods: (a) by immersing the freshly prepared sample in 1 mM H_2PtCl_4/0.1 M $HClO_4$ at −100 mV until the amount of charge transferred through the system corresponded to the desired amount of deposited platinum within an accuracy of 10%; (b) by immersing at 0.4 V and cycling the potential between 0.4 and −0.15 V at 50 mV s^{-1} followed by emersion at 0.4 V. After the dry emersion procedure, the electrode was rinsed with pure water. The modified surfaces are referred to according to (a) the deposition method, either as PS (potentiostatic deposition) or PD (potentiodynamic deposition) and (b) the amount of deposited monolayers in the first case (PS) or the number of cycles of deposition in the second case (PD). The potentiodynamic deposition method does not allow a reliable means of evaluation of the amount of charge deposited because the CVs recorded during the deposition showed a large background current due to the oxide formation/reduction and no particular peak that could be associated with the Pt deposition.

The LEED pattern for the Ru(10$\bar{1}$0) electrodes with various Pt coverages exhibits always a (1 × 1) phase, while the additional reflection spots 200, 220, 311 due to the Pt deposit, which are calibrated from the substrate unit vector $b_{10,}$ can only be observed in RHEED, shown in Fig. 5(a) and (b) for the 4 ML PS and five-cycles PD modified surfaces, respectively. The additional spots with the intensity-extension perpendicular to the Ru surface indicate that the Pt deposit forms a thin layer of patches dispersed on Ru(10$\bar{1}$0) in the case of the PS surfaces. On the other hand, the radial streaking of the 3D spots for the PD surfaces indicates that the Pt particles are tilted with respect to the substrate surface. Based on the intensity profile of the reflection spots, the Pt on the PS samples apparently forms numerous patches with thickness of 3–4 layers and a mean domain size of *ca.* 12 nm on the Ru(10$\bar{1}$0) surface. The corresponding SEM images for the for the 4 ML PS and five-cycles PD modified surfaces are reproduced in Fig. 5(e) and (f), respectively. The SEM image shows a size distribution of 5–12 nm where the Ru electrode is *ca.* 80–90% covered by Pt patches for the 4 ML PS sample. The thickness of the Pt patches increases with increasing Pt deposition, which is demonstrated by the reduced spot-extension perpendicular to the sample surface as seen in the RHEED pattern for 4 ML PS compared with that for the 2 ML PS. In the case of potentiodynamic deposition, after five deposition cycles the Ru(10$\bar{1}$0) electrode surface is approximately 50% covered with the Pt deposit (Fig. 5(f)). The corresponding Auger spectra for the Pt modified-Ru(10$\bar{1}$0) surfaces, for several platinum contents, obtained by the two deposition methods are displayed in Fig. 6(a), where the number of monolayers (cycles) indicates the extent of the potentiostatic (potentiodynamic) deposition. In general, an increased Pt Auger signal at 64 eV and the decreased Ru Auger signal (272 eV) with increasing Pt deposit can be seen for both deposition methods. Obviously the epitaxial growth of the Pt deposit on Ru(10$\bar{1}$0) proceeds *via* a VOLMER-WEBER growth mode.[32] In all cases, the chlorine signal can be observed even after rinsing of the sample, indicating that this signal is probably due to strongly bonded chloride which is a by-product of the platinum deposition. The chloride interference was eliminated in the further electrochemical experiments due to displacement by CO. Fig. 6(b) presents the CV for the two-cycles PD modified Ru(10$\bar{1}$0). The dotted curve represents the CV in 0.1 M $HClO_4$ after the Pt deposition and characterization in the UHV chamber. The solid curve represents the first and second cycle for the CO stripping experiment. The presence of chloride before the CO adsorption inhibits the pseudo-capacitive processes associated with hydroxide/oxide formation for potentials more positive than −0.1 V, which can be recovered after the chloride removal. The processes below this potential are unaffected by the presence of chloride. This region features a peak around −0.15 V probably associated with hydrogen desorption from platinum.

Closer inspection of the RHEED pattern at the [0001] azimuth illustrated in Fig. 5(a) shows that the spot-spacing

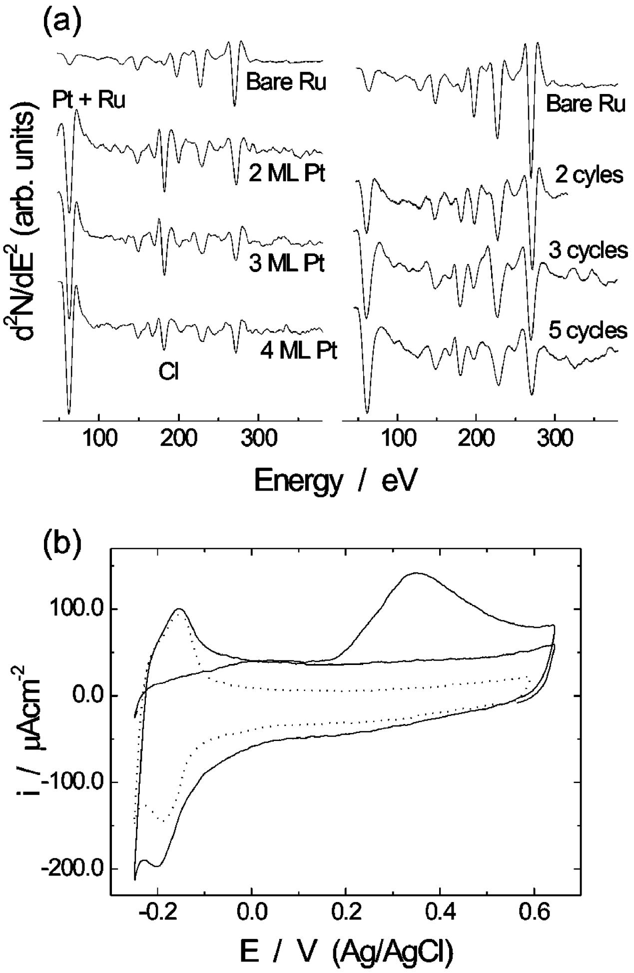

Fig. 6 Auger spectra for the clean and Pt-modified Ru(10$\bar{1}$0) (a). Cyclic voltammogram for the two-cycles PD modified surface in 0.1 M $HClO_4$ immediately after Pt deposition (--) and after the CO electrosorption at −0.2 V (—) (b). Scan rate 50 mV s^{-1}.

between the 3D spot and 00 beam along the specular beam is 0.841 A^{-1} (calibrated from the unit vector b_{10} − 0.369 A^{-1}), corresponding to the 311 reflection (0.8453 A^{-1}) of Pt, and for all azimuth-rotations it remains always at the specular beam (Fig. 5(c)), demonstrating that the Pt clusters grow with their (311) plane parallel to the Ru(10$\bar{1}$0) substrate surface. The 200 and 002 spots of Pt overlap at smaller incident angle with the (0,1) and (0,1) substrate reflection streaks, respectively, suggesting that the [233] atomic rows of the Pt(311) plane are parallel to the [0001] atomic rows of the Ru(10$\bar{1}$0) surface, which is demonstrated by the proposed model in the schematic drawing in Fig. 7. With azimuthal rotation of 17.6° from the [0001] direction, additional reflection spots 113, 13$\bar{1}$ due to Pt clusters appear between the (00) and ±(21) beams, as expected (see Fig. 5(c)). These reflections are absent on the bare Ru(10$\bar{1}$0) surface, shown in Fig. 5(d), because no reciprocal lattice rod intersects with the Ewald sphere. This provides strong evidence that the [011] rows of Pt(311) are compressed by 3.2% with respect to the bulk Pt in order to match with the ($\bar{1}2\bar{1}0$) rows of the Ru(10$\bar{1}$0) surface (see Fig. 7). As a result of the [01$\bar{1}$] row-matching with the [$\bar{1}2\bar{1}0$] rows, the [$\bar{2}$33] row spacing of the (311) plane perpendicular to the [0$\bar{1}$1] rows fits with the [0001] row spacing of the Ru(10$\bar{1}$0) surface, which is confirmed by the RHEED patterns obtained at the [0001] azimuth in Fig. 5(a) and (b), in which the additional reflection spots 220 of Pt overlap with the substrate reflection streaks.

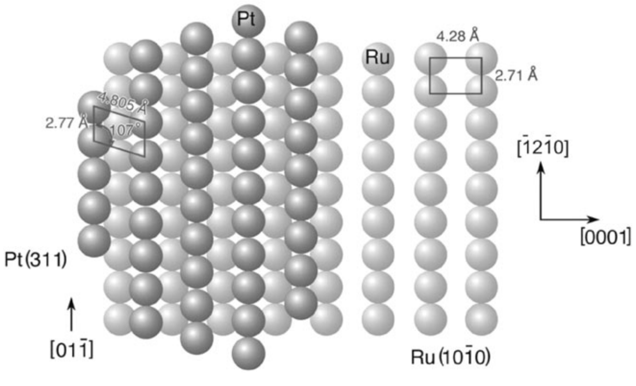

Fig. 7 Model for the Pt adlayer in direct contact with the Ru(10$\bar{1}$0) surface.

CO and methanol oxidation on the modified Ru surfaces

The cyclic voltammograms of the Pt-modified Ru(10$\bar{1}$0) for several coverages obtained from both deposition methods are presented in Fig. 8(a). In Fig. 8(b), for the purpose of correlation, the plots of the intensity ratios of the peak at 64 eV to the peak at 272 eV in the Auger spectra are shown. The potentiodynamic deposition (0.4 to −0.15 V) seems to produce a very rough surface compared with the potentiostatic deposition. This could be anticipated by the characteristics of the deposits as discussed above. This is probably a consequence of holding the potential above 0.3 V before/after the deposition. The two methods of deposition lead also to a very different CV profiles in the hydrogen desorption region, which has to be related primarily to the morphology of the deposited Pt particles. In particular, the 2 ML PS and the five-cycles PD surfaces would provide a good basis for comparison as they both show approximately the same Ru/Pt Auger peak ratio.

In general, a larger fraction of the Ru(10$\bar{1}$0) surface is covered with Pt for the PS surfaces than the PD surfaces because the former method yields thinner deposits than the latter. This is demonstrated by the fact that the RHEED pattern of the potentiostatically modified Ru in Fig. 5 shows a larger intensity extension perpendicular to the surface than the potentiodynamically modified Ru and also a larger Auger peak ratio (Fig. 8(b)). Additionally, in this case of PS surfaces, the CV profiles do not seem at first to change considerably in the hydrogen region with the increasing amount of platinum. It has to be kept in mind, however, that processes on bare ruthenium also contribute to the current in this potential region and the increasing current due to platinum processes might partially be compensated by the decreasing current due to ruthenium processes. The increased amount of platinum is made evident by the larger current in the cathodic scan at 0.55 V corresponding to the reduction of platinum (hydro)oxide and the decrease of the current related to the reduction of ruthenium oxide at 0.1 V. The same analysis cannot be applied to the case of the deposition by cycling due to the lack of control of the extent of roughening/disordering undergone by the uncovered ruthenium part, but in this case, the increase in the current in the hydrogen UPD region on platinum can be verified. The suppression of the H-upd signal observed in the case of the PS surfaces is in perfect agreement with a recent work on Pt–Ru(0001)[36] and is explained by the weaker Pt–H bonding due to electronic effects provided by the Pt lattice compression, which will be discussed in the next section.

The CO stripping curves for the Pt-modified surfaces under consideration are shown in Fig. 9. In general, the CO oxidation occurs at lower potentials (about 50 mV) with respect to the bare Ru(10$\bar{1}$0). In the case of the more rough PD surfaces, the peak potential is observed at approximately 0.34 V and shows no major dependence on the amount of platinum on the surface. The peak potential is, in fact, very similar to that of the bare roughened ruthenium surface (Fig. 3(b)) and the catalytic enhancement is probably due to roughening and

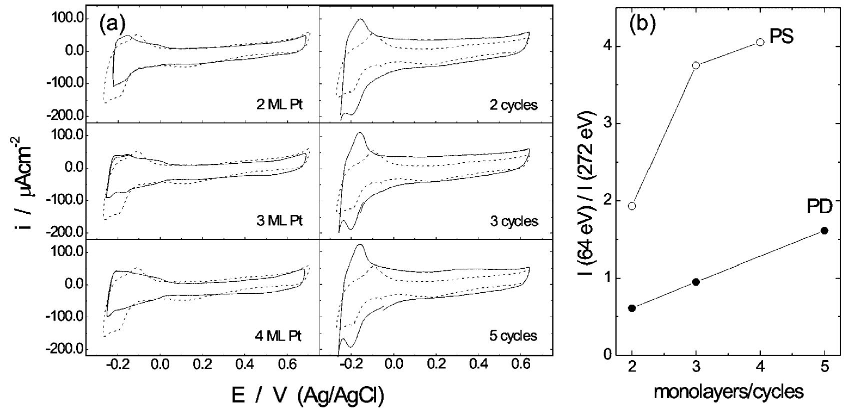

Fig. 8 Cyclic voltammograms of the Pt-modified Ru(10$\bar{1}$0) surfaces in 0.1 M $HClO_4$ (a); the cyclic voltammogram of the bare Ru(10$\bar{1}$0) is shown in the dashed line. Scan rate 50 mV s^{-1}. Intensity of the Auger signal at 64 eV (from Pt and Ru) relative to the signal at 272 eV (from Ru) for the Pt-modified Ru(10$\bar{1}$0) surfaces.

disordering, at least on the Pt free sites. The amount of oxidized CO appears to be almost the same. Again, it must be taken into account that, by increasing the amount of platinum, the ruthenium oxide formation (after CO stripping) occurs to a lesser extent. This can be clearly seen by the fact that the oxidation peak becomes sharper upon increasing the amount of platinum. This means that the overall current remains almost the same while a lesser contribution comes from the further ruthenium oxidation (thus a greater relative contribution from CO oxidation) as the Pt amount increases. In all cases only a single oxidation peak is observed, thus, there is no evidence of the reaction involving energetically different adsorption sites for oxygen containing species or CO. Single peaked waves for the CO oxidative stripping have so far been observed for PtRu alloys where the Pt–Ru intermixing occurs at an atomic level, whereas by phase segregation induced by annealing, multi-peaked waves are observed.[21] The SEM images of Fig. 5(e) and (f) clearly show that the surfaces under consideration are composed of segregated Pt and Ru phases. Consequently, either the oxidation of CO on the platinum-covered part of the surface occurs at lower potentials if compared with smooth Pt or the CO diffusion from platinum adsorption sites to oxygen containing Ru sites is very fast.

As indicated by RHEED analysis and the SEM images, the platinum particles are relatively large and comprise several layers for the case of the potentiodynamic deposition. Consequently, fast CO diffusion would be unlikely to occur as the particles must contain relatively large amounts of kinks and steps that would hinder CO diffusion. This fact also makes it difficult to accept that the ruthenium substrate can cause pronounced electronic effects in large particles of more than, for example, 12 ML thick. One possible explanation would be the high concentration of defects in the Pt nanoparticles. The CO stripping profiles are very similar for the case of two monolayer potentiostatic deposition and of five cycles potentiodynamic deposition in the potential range above 0.2 V, despite the differences in the roughness of the substrate. This again can be rationalized in terms of the amount of uncovered ruthenium still available for further oxidation after CO stripping because they present the same surface coverage.

In the case of the potentiostatic deposition, the general trend of sharpening the peak can be still observed from 2 to 4 ML, but for the case of the three and four monolayer deposits, the peak potential becomes shifted negatively by a further 40 mV. These two surfaces show similar Pt/Ru Auger peak ratios, indicating only the uniform epitaxial growth of the Pt deposit at a coverage saturation of 80 to 90%. In the case of the 2 ML, the coverage is estimated to be about 50% based on the similarity of the Pt/Ru peak ratio of this surface and of that obtained by five cycles of potentiodynamic deposition. This indicates that in this case the Pt patches are slightly more active than the uncovered Ru part of the surface. The potentiostatically deposited platinum forms more ordered layers and the improved catalytic activity cannot be rationalized in terms of surface defects alone. The improvement in the catalytic activity of the Pt deposits may be related to electronic effects as the potentiostatic deposition provides considerably more ordered and thinner deposits (3–4 ML thick). This enhancement by the electronic effect for thin Pt deposits may be due to the Pt lattice compression.[35,36] For thin Pt layers, the Pt–Pt distance at the outermost layer is still different from the bulk value. For thicker layers, the Pt–Pt distance in the outermost layers is similar to the bulk value as the lattice distortion spans only through the few first layers.

If the CO stripping curves do not show remarkable differences for the studied surfaces, the activity towards methanol oxidation shows great dependence on the structural characteristics and amount of platinum. It is known that Ru is not active for methanol oxidation due to its inability to adsorb and dehydrogenate methanol in acidic media at low temperature.[24,53,58] Thus, the differences in activity for this reaction can be discussed in terms of two main effects: activity of the platinum deposits for the dehydrogenation step and the overall catalytic activity of the binary system to oxidize the CO intermediate. This latter is more important in the case of methanol oxidation with respect to the CO oxidation because, in principle, no CO formation is expected to occur at the Ru sites due to its inability to adsorb/dehydrogenate methanol. This leaves the Ru sites free for the formation of oxygenated

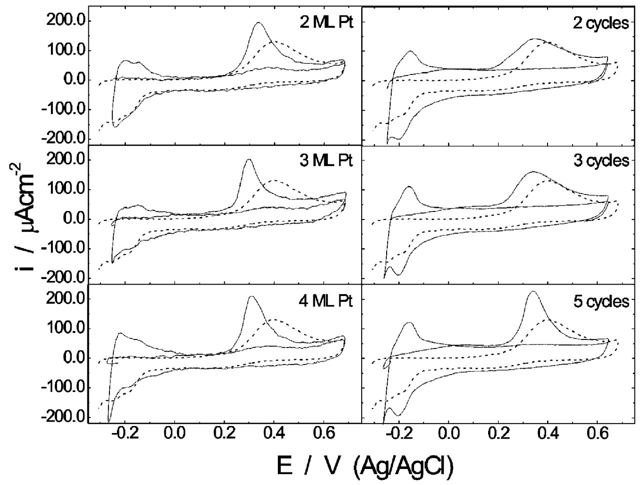

Fig. 9 CO oxidative stripping on the Pt-modified Ru(10$\bar{1}$0) surfaces in 0.1 M $HClO_4$; the stripping curve for the bare Ru(10$\bar{1}$0) is shown in the dashed line. Scan rate 50 mV s^{-1}.

species. Thus, a bi-functional mechanism can be expected in this case, with the Ru sites providing the oxygenated species. The CVs for the PD and PS surfaces in 0.1 M CH_3OH + 0.1 M $HClO_4$ are shown in Fig. 10(a) and (b), respectively. For comparison, in Fig. 10(c) the positive going scans after subtraction of the current value at 0 V for all the surfaces under consideration are shown. In the case of the PD surfaces, low or no activity towards methanol oxidation is observed except for the Pt modified surface with five deposition cycles. The difference in activity does not follow the linear relation observed in the Pt/Ru peak ratio in the Auger spectra, which should reflect the effective Pt coverage. This indicates that the main factor determining the variations in catalytic activity between these surfaces is the differences in the density of Ru-Pt domain boundaries. Notice that in this case, the density of defects in the particle size is expected to be high for all PD surfaces, as discussed for the CO stripping experiments. It seems that the major contribution to the overall methanol oxidation comes from the dehydrogenation of methanol at the Pt sites followed by the oxidation of the CO intermediate along the perimeter of the Pt domains, by reaction with oxygenated species formed at the Ru sites. The surface formed by five deposition cycles exhibited more activity towards methanol oxidation than that with two monolayers of potentiostatically deposited platinum. These two surfaces exhibit very similar Pt/Ru auger peak ratios and activity towards CO oxidation. Consequently, the observed difference cannot be rationalized in terms of optimal Pt/Ru ratio. The fact that the potentiodynamically deposited surface might be slightly rougher does not account for the twice as high current observed for this surface. The difference in activity is probably related to the greater density of defects which serve as possible centers for the methanol dehydrogenation in the platinum domains. These defects also enhance the adsorption of oxygenated species as a similar activity towards CO oxidation was observed for these two surfaces. Therefore, the predominant factor in this particular case comes from a larger contribution of the methanol dehydrogenation reaction in the more irregular nanoparticles obtained by potentiodynamic deposition. Yet, this latter surface exhibits inferior activity to those with three and four Pt monolayers potentiostatically deposited. In this case, these smoother potentiostatically deposited Pt-modified surfaces may feature a lesser number of defects, but the determining factor for the enhanced activity seems to be the greater ability to oxidize the CO intermediate along the perimeter of the Pt nanoparticles through a real bi-functional mechanism. Notice that the current drop after the oxidation peak occurs at more positive potentials for the surfaces with 3 and 4 ML Pt compared with the potentiodynamic deposited surface. This is a reflection of the presence of strongly adsorbed oxygenated species in the Pt sites at positive potentials, leading to inhibition of methanol adsorption/dehydrogenation. In the case of the potentiodynamically modified surface the pathway involving oxygenated species formed at the defects of Pt sites gives an important contribution to the overall process. On the other hand, the same factor leads to the poisoning by strongly adsorbed oxygenated species at Pt sites at lower potentials if compared with the smoother potentiostatically modified surfaces.

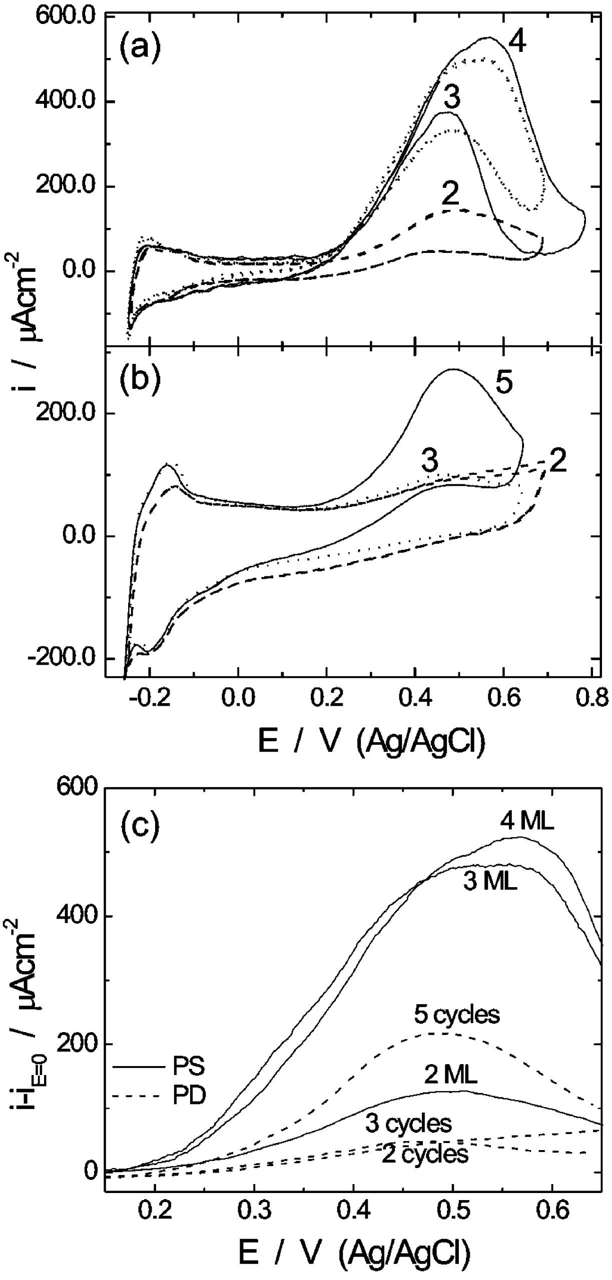

Fig. 10 Cyclic voltammograms in 0.1 M CH_3OH + 0.1 M $HClO_4$ for the potentiostatically (a) and potentiodynamically (b) Pt-modified Ru(10$\bar{1}$0) surfaces. Positive going scans for the cyclic voltammograms in (a) and (b) after subtraction of the current density at 0 V (c). Scan rate 50 mV s^{-1}.

Conclusions

The electrooxidation of CO and methanol on Ru(10$\bar{1}$0) and Pt-modified Ru(1010) electrodes was conducted in 0.1 M $HClO_4$ and CH_3OH-containing solutions. The Pt deposit grows with its (311) plane parallel to the Ru(10$\bar{1}$0) substrate surface, forming patches with size distribution which depends on the potential control during the deposition. This dependence is due to the fact that the substrate surface features differing structural characteristics for different potentials. The epitaxial growth of Pt deposit proceeds *via* a Volme–Weber growth mode, for which the bare Ru(10$\bar{1}$0) surface and the Pt patches are coexisting.

The onset potential for the oxidation of CO on the Ru(1010) electrodes is significantly lower than that on the bare Pt and bare Ru(0001), which indicates higher catalytic activity. The driving force for the high reactivity on Ru(10$\bar{1}$0) is most likely due to the low oxidation potential for Ru atoms with low coordinated bonding on Ru(10$\bar{1}$0) which leads to surface disordering as demonstrated by the LEED pattern for the Ru(10$\bar{1}$0) electrode in which the streak-spots that were observed prior to CO oxidation are no longer visible afterwards.

CO_{ad} electrooxidation on the Pt-modified Ru(10$\bar{1}$0) electrode surfaces is shifted toward more negative potential compared with the bare Ru(10$\bar{1}$0) surfaces indicating higher reactivity. The catalytic enhancement for the Pt/Ru(10$\bar{1}$0) electrodes is attributed to the electronic effect due to the strain caused by adlayer lattice compression as well as the increase in the concentration of surface defects.

The most important effect for the enhancement of catalytic activity towards methanol electrooxidation on the deposited Pt–Ru($10\bar{1}0$) system is the bi-functional mechanism with the CO intermediate species being oxidized at the Pt /Ru perimeter. The maximum activity observed in this study was for the 4 ML potentiostatically deposited Pt, where the Ru surface is *ca.* 80–190% covered with the Pt patches.

Acknowledgements

The authors would like to express their gratitude to Gisela Weinberg for the SEM experiments and to the Max Planck Society for the financial support. A. L. N. P. is grateful to Dr Lei Ting for the introduction to the experimental procedures.

References

1 W. Vielstich, A. Lamm and H. Gasteiger, *Handbook of Fuel Cells: Fundamentals, Technology, Applications*, John Wiley & Sons Ltd, Chichester, 2003.
2 Z. Jusys, J. Kaiser and R. J. Behm, *Electrochim. Acta*, 2002, **47**, 3693.
3 E. A. Batista, H. Hoster and T. Iwasita, *J. Electroanal. Chem.*, 2003, **554**, 265.
4 T. Diemant, T. Hager, H. E. Hoster, H. Rauscher and R. J. Behm, *Surf. Sci.*, 2003, **541**, 137.
5 W. H. Lizcano-Valbuena, V. A. Paganin, C. A. P. Leite, F. Galembeck and E. R. Gonzalez, *Electrochim. Acta*, 2003, **48**, 3869.
6 A. A. El-Shafei, R. Hoyer, L. A. Kibler and D. M. Kolb, *J. Electrochem. Soc.*, 2004, **151**, F141.
7 C. Lu and R. I. Masel, *J. Phys. Chem. B*, 2001, **105**, 9793.
8 J. C. Davies, B. E. Hayden and D. J. Pegg, *Surf. Sci.*, 2000, **467**, 118.
9 G.-Q. Lu, P. Waszczuk and A. Wieckowski, *J. Electroanal. Chem.*, 2002, **532**, 49.
10 W. F. Lin, M. S. Zei, M. Eiswirth, G. Ertl G, T. Iwasita and W. Vielstich, *J. Phys. Chem. B*, 1999, **103**, 6968.
11 M. S. Zei, T. Lei and G. Ertl, *Z. Phys. Chem.*, 2003, **217**, 447.
12 H. Hoster, T. Iwasita, H. Baumgartner and W. Vielstich, *J. Electrochem. Soc.*, 2001, **148**, 1896.
13 T. Iwasita, H. Hoster, A. John-Anacker, W. F. Lin and W. Vielstich, *Langmuir*, 2000, **16**, 522.
14 H. Hoster, T. Iwasita, H. Baumgartner and W. Vielstich, *Phys. Chem. Chem. Phys.*, 2001, **3**, 337.
15 S. R. Brankovic, N. S. Marinkovic, J. X. Wang and R. R. Adzic, *J. Electroanal. Chem.*, 2002, **532**, 57.
16 B. E. Hayden, M. E. Rendall and O. South, *J. Am. Chem. Soc.*, 2003, **125**, 7738.
17 E. I. Santiago, G. A. Camara and E. A. Ticianelli, *Electrochim. Acta*, 2003, **48**, 3527.
18 E. I. Santiago, M. J. Giz and E. A. Ticianelli, *J. Solid State Electron.*, 2003, **7**, 607.
19 M. Watanabe and S. Motoo, *J. Electroanal. Chem.*, 1975, **60**, 267.
20 M. Watanabe and S. Motoo, *J. Electroanal. Chem.*, 1975, **60**, 275.
21 H. A. Gasteiger, N. Markovic, P. N. Ross and E. J. Cairns, *J. Phys. Chem.*, 1994, **98**, 617.
22 H. A. Gasteiger, N. Markovic, P. N. Ross and E. J. Cairns, *J. Phys. Chem.*, 1995, **99**, 8290.
23 W. F. Lin, T. Iwasita and W. Vielstich, *J. Phys. Chem. B*, 1999, **103**, 3250.
24 H. A. Gasteiger, N. Markovic, P. N. Ross and E. J. Cairns, *J. Phys. Chem.*, 1993, **97**, 12020.
25 M. Christov and K. Sundmacher, *Surf. Sci.*, 2003, **547**, 1.
26 T. Iwasita, *Electrochim. Acta*, 2002, **47**, 3663.
27 F. Buatier de Mongeot, M. Scherer, B. Gleich, E. Kopatzki and R. J. Behm, *Surf. Sci.*, 1998, **411**, 249.
28 B. Hammer and J. K. Nørskov, *Surf. Sci.*, 1995, **343**, 211.
29 B. Hammer, Y. Morikawa and J. K. Nørskov, *Phys. Rev. Lett.*, 1996, **76**, 2141.
30 B. Hammer, O. H. Nielsen and J. K. Nørskov, *Catal. Lett.*, 1997, **46**(1997), 31.
31 T. E. Shubina and M. T. M. Koper, *Electrochim. Acta.*, 2002, **47**, 3621.
32 J. A. Rodriguez, *Surf. Sci. Rep.*, 1996, **24**, 223.
33 A. Logadottir and J. K. Nørskov, *Surf. Sci.*, 2001, **489**, 135.
34 J. Meier, J. Shiøtz, P. Liu, J. K. Nørskov and U. Stimming, *Chem. Phys. Lett.*, 2004, **390**, 440.
35 A. Schlapka, M. Lischka, A. Groß, U. Kärsberger and P. Jakob, *Phys. Rev. Lett.*, 2003, **91**, 016101.
36 H. Hoster, B. Richter and R. J. Behm, *J. Phys. Chem. B*, 2004, **108**, 14780.
37 W. F. Lin, M. S. Zei, Y. D. Kim, H. Over and G. Ertl, *J. Phys. Chem. B*, 2000, **104**, 6040.
38 H. Inoue, S. R. Brankovic, J. X. Wang and R. R. Adzic, *Electrochim. Acta*, 2002, **47**, 3777.
39 H. Inoue, J. X. Wang, K. Sasaki and R. R. Adzic, *J. Electroanal. Chem.*, 2003, **554**, 77.
40 G. Rotaris, A. Baraldi, G. Comelli, M. Kiskinova and R. Rosei, *Surf. Sci.*, 1996, **359**, 1.
41 J. P. R. Symonds, H. Arnolds, V. L. Zhang, K. Fukutani and D. A. King, *J. Chem. Phys.*, 2004, **120**, 7158.
42 S. Schwegmann, A. P. Seitsonen, V. De Renzi, H. Dietrich, H. Bludau, M. Gierer, H. Over, K. Jacobi, M. Scheffler and G. Ertl, *Phys. Rev. B*, 1998, **57**, 15487.
43 A. Baraldi, S. Lizzit and G. Paolucci, *Surf. Sci.*, 2000, **457**, 1.
44 A. Baraldi, S. Lizzit, G. Comelli and G. Paolucci, *Phys. Rev. B*, 2001, **63**, 115410-1.
45 Y. D. Kim, S. Schwegmann, A. P. Seitsonen and H. Over, *J. Phys. Chem. B*, 2001, **105**, 2205.
46 S. Wendt, A. P. Seitsonen and H. Over, *Catal. Today*, 2003, **85**, 167.
47 H. Over and M. Muhler, *Prog. Surf. Sci.*, 2003, **72**, 3.
48 M. S. Zei and G. Ertl, *Phys. Chem. Chem. Phys.*, 2000, **2**, 3855.
49 W. F. Lin, P. A. Christensen, A. Hamnett, M. S. Zei and G. Ertl, *J. Phys. Chem. B*, 2000, **104**, 6642.
50 N. S. Marinkovic, J. X. Wang, H. Zajonz and R. R. Adzic, *Electrochem. Solid St.*, 2000, **3**, 508.
51 W. B. Wang, M. S. Zei and G. Ertl, *Phys. Chem. Chem. Phys.*, 2001, **3**, 3307.
52 J. X. Wang, N. S. Marinkovic, H. Zajonz, B. M. Ocko and R. R. Adzic, *J. Phys. Chem. B*, 2001, **105**, 2809.
53 W. F. Lin, P. A. Christensen and A. Hamnett, *Phys. Chem. Chem. Phys.*, 2001, **3**, 3312.
54 J. Lee, W. B. Wang, M. S. Zei and G. Ertl, *Phys. Chem. Chem. Phys.*, 2002, **4**, 1393.
55 W. B. Wang, M. S. Zei and G. Ertl, *Chem. Phys. Lett.*, 2002, **355**, 301.
56 A. M. El-Aziz and L. A. Kibler, *Electrochem. Comm.*, 2002, **4**, 866.
57 T. Lei, J. Lee, M. S. Zei and G. Ertl, *J. Electroanal. Chem.*, 2003, **554–555**, 41.
58 W. F. Lin, J. M. Jin, P. A. Christensen and K. Scott, *Electrochim. Acta*, 2003, **48**, 3815.
59 J. M. Jin, W. F. Lin and P. A. Christensen, *J. Electroanal. Chem.*, 2004, **563**, 71.
60 C. S. McKee, D. L. Perry and M. W. Roberts, *Surf. Sci.*, 1973, **39**, 176.
61 W. Braun, *Applied RHEED, Springer Tracts in Modern Physics*, Springer, Berlin, 1999.